CrossMark

Parametric Study of Urban-Like Topographic Statistical Moments Relevant to a Priori Modelling of Bulk Aerodynamic Parameters

Xiaowei Zhu[1] · **G. Valerio Iungo[1]** · **Stefano Leonardi[1]** ·
William Anderson[1]

Abstract For a horizontally homogeneous, neutrally stratified atmospheric boundary layer (ABL), aerodynamic roughness length, z_0, is the effective elevation at which the streamwise component of mean velocity is zero. A priori prediction of z_0 based on topographic attributes remains an open line of inquiry in planetary boundary-layer research. Urban topographies – the topic of this study – exhibit spatial heterogeneities associated with variability of building height, width, and proximity with adjacent buildings; such variability renders a priori, prognostic z_0 models appealing. Here, large-eddy simulation (LES) has been used in an extensive parametric study to characterize the ABL response (and z_0) to a range of synthetic, urban-like topographies wherein statistical moments of the topography have been systematically varied. Using LES results, we determined the hierarchical influence of topographic moments relevant to setting z_0. We demonstrate that standard deviation and skewness are important, while kurtosis is negligible. This finding is reconciled with a model recently proposed by Flack and Schultz (J Fluids Eng 132:041203-1–041203-10, 2010), who demonstrate that z_0 can be modelled with standard deviation and skewness, and two empirical coefficients (one for each moment). We find that the empirical coefficient related to skewness is not constant, but exhibits a dependence on standard deviation over certain ranges. For idealized, quasi-uniform cubic topographies and for complex, fully random urban-like topographies, we demonstrate strong performance of the generalized Flack and Schultz model against contemporary roughness correlations.

Keywords Aerodynamic drag · Large-eddy simulation · Roughness length ·
Urban topography

✉ William Anderson
  wca140030@utdallas.edu

[1] Mechanical Engineering Department, University of Texas at Dallas, Richardson, TX, USA

1 Introduction

The atmospheric boundary layer (ABL) is directly influenced by the Earth's surface via the surface fluxes of momentum, heat, and humidity (Garratt 1994; Wyngaard 2010; Lee and Wu 2015). At regional scales (Bou-Zeid et al. 2007), the cumulative effect of flow separation on obstacles (terrain undulations, vegetation, and urban obstacles) is responsible for aggregate surface momentum fluxes (aerodynamic drag). For neutrally stratified, statistically horizontally homogeneous (Belcher et al. 2012) conditions, the atmospheric surface layer is vertically composed of a roughness sublayer and inertial layer (Harmon and Finnigan 2007). The roughness sublayer, which constitutes the rough-wall counterpart of the viscous sublayer over 'smooth walls' (Raupach et al. 1991), is of importance when modelling flow or dispersion processes in urban environments (Rotach 1999; Roth 2000). The roughness sublayer depth, z_{RSL}, scales linearly with the aggregate obstacle elevation, $\langle h_o \rangle$, where $3 \leq z_{\mathrm{RSL}}/\langle h_o \rangle \leq 5$ is commonly cited (Harmon and Finnigan 2007; Böhm et al. 2013; Anderson et al. 2015b) and $\langle . \rangle$ denotes a spatial average.[1] Within the roughness sublayer, the mean flow exhibits spatial variability associated with geometric attributes of topographic elements, while above this (in the inertial layer) the mean flow (streamwise velocity component) tends to a logarithmic profile and turbulence structural attributes are unaffected by the topography (Townsend 1976). For fully rough conditions (Raupach et al. 1991; Kanda et al. 2004; Coceal et al. 2006; Kanda 2006; Coceal et al. 2007) resembling the ABL, and under the aforementioned statistically horizontally homogeneous conditions, the law of the wall (Tennekes and Lumley 1972) yields the equilibrium logarithmic law,

$$\frac{U(z)}{u_*} = \frac{1}{\kappa} \ln \left[\frac{z - d}{z_0} \right], \tag{1}$$

where $U(z)$ is the temporally- and spatially-averaged streamwise velocity component at surface-normal elevation, z, u_* is the friction velocity (defined by $u_* = (\tau^w/\rho)^{1/2} = \langle u'w' \rangle_t^{1/2}$, where τ^w is the wall stress, u and w are the streamwise and vertical velocity components, respectively, $\langle \ldots \rangle_t$ denotes a time average, and superscript 'prime' denotes a deviation from the Reynolds average), κ is the von Kármán constant ($\approx$0.41, Pope 2000), d is the zero-plane displacement (Castro 2007), and z_0 is the aerodynamic roughness length (Lettau 1969; Raupach et al. 1991; Macdonald et al. 1998; Jimenez 2004; Napoli et al. 2008; Schultz and Flack 2009; Flack and Schultz 2010; Anderson and Meneveau 2010, 2011). Physically (see Eq. 1), z_0 is the effective height at which $U(z) = 0$, while d is interpreted as the elevation at which the mean surface drag acts (Jackson 1981; Placidi and Ganapathisubramani 2015). In the context of Eq. 1, increasing z_0 manifests a momentum deficit, $\delta U(z)$, associated with increasing aerodynamic drag. Displacement height, d, on the other hand, modifies the slope of the logarithmic-linear $U(z)$ profile, and scales linearly with $\langle h_o \rangle$ (Thom 1971; Jackson 1981; Cheng and Castro 2002; Kanda et al. 2004; Coceal et al. 2006; Kanda 2006), where $d/\langle h_o \rangle \approx 0.75$ is commonly adopted (Gardner 2004). Note also that Eq. 1 can be re-written to yield surface stress with respect to the prevailing pressure gradient forcing, $\mathrm{d}p_0/\mathrm{d}x$, associated with the geostrophic balance,

---

[1] The function representing a given topography, $h(x, y)$, contains zeros at spatial positions, $\{x, y\}$, where there are no obstacles. The variable $\langle h_o \rangle = \varphi \langle h(x, y) \rangle$, where $\varphi = N_x N_y / \sum_i^{N_x} \sum_j^{N_y} I(x_i, y_j)$, N_x and N_y are the number of computational points in the x- and y-directions, respectively, and $I(x, y) = \mathcal{H}\left[h(x, y) - \delta_z/2 \right]$ is an indicator function, where $\mathcal{H}[x]$ is the Heaviside step function and $\delta_z/2$ is the height of the first node in the staggered grid computational mesh.

Table 1 Survey of existing z_0 models from the boundary-layer meteorology community

Citation	Argument(s)	$\dfrac{z_0}{\langle h_o \rangle}$	$\dfrac{d}{\langle h_o \rangle}$
Kutzbach (1961)	$\langle h_o \rangle, \lambda_f$	$0.5\lambda_f$	-
Lettau (1969)			
Wooding et al. (1973)			
Counehan (1971)	$\langle h_o \rangle, \lambda_p$	$1.08\lambda_p - 0.08$	–
Fang and Sill (1992)	$\langle h_o \rangle$	0.1	–
Theurer (1993)	$\langle h_o \rangle, \lambda_f, \lambda_p$	$1.6\lambda_f(1 - 1.67\lambda_p)$	$1.67\lambda_p$

$$\frac{\tau^w}{\rho} = u_*^2 = -\left[\frac{\kappa U(z)}{\ln\left(\{z-d\}/z_0\right)}\right]^2 = \frac{H}{\rho}\frac{\mathrm{d}p_0}{\mathrm{d}x}. \tag{2}$$

Given the physical definition of z_0 (embodied in Eq. 1), it follows that a unique z_0 exists for each topography; z_0 can be found a posteriori via experimental measurement, whereby the Reynolds-averaged velocity profile is used to infer z_0. The practical limitations on this approach are obvious, which has motivated development of prognostic models. A priori estimation of z_0 based only on geometric details of the topography is an open research effort in boundary-layer meteorology. Models for z_0 play an important role in numerical weather prediction and generating realistic inflow conditions for simulations of ABL turbulence (Macdonald et al. 1998; Armenio et al. 2010; Flack and Schultz 2010). Predictive models have been proposed, and below we provide a brief survey of this work. In all cases, a unifying theme is the use of geometric details of the topography in roughness correlations.

1.1 Boundary-Layer Meteorology

In the boundary-layer meteorology community, predictive models for z_0 are commonly based on scaling arguments with $\langle h_o \rangle$, frontal area index,

$$\lambda_f = \frac{A_f}{A_d}, \tag{3}$$

and plan area index,

$$\lambda_p = \frac{A_p}{A_d}, \tag{4}$$

where A_f, A_d, and A_p are, respectively, the total frontal area of obstacles, total surface area, and total area covered by obstacles (Lettau 1969; Macdonald et al. 1998; Grimmond and Oke 1999). Substantial work has been done to estimate the correlations for $z_0 = z_0(\langle h_o \rangle, \lambda_f, \lambda_p)$ (Millward-Hopkins et al. 2011; Placidi and Ganapathisubramani 2015). Table 1 is a brief survey of pre-Macdonald et al. (1998) z_0 models, shown in chronological order to highlight the generalizations that have been made to attain greater reliability (Lettau 1969; Hansen 1992; Fang and Sill 1992; Garratt 1994; Macdonald et al. 1998).

Following the models presented in Table 1, most of which were limited to low roughness element densities and do not account for the non-linear decrease in z_0 for high roughness densities, Macdonald et al. (1998) introduced a greatly generalized (larger range for λ_p) correlation for arrays of uniform height blocks. Macdonald et al. (1998) proposed,

$$\frac{z_0}{\langle h_o \rangle} = \left(1 - \frac{d}{\langle h_o \rangle}\right) \exp\left\{-\left[\frac{\beta \lambda_f}{2} \frac{C_D}{\kappa^2}\left(1 - \frac{d}{\langle h_o \rangle}\right)\lambda_f\right]^{-\frac{1}{2}}\right\},\tag{5}$$

where $d/\langle h_o \rangle = 1 + A^{-\lambda_p}(\lambda_p - 1)$, and $C_D = 1.2$ is a pre-defined drag coefficient for the obstacles. For uniform-height staggered building arrays, the parameters required for application of Eq. 5 are $A = 4.43$ and $\beta = 1.0$. The Macdonald et al. (1998) model appears to be most widely used as it incorporates a broader range of scenarios relative to other methods (Kanda and Moriizumi 2009; Millward-Hopkins et al. 2011; Placidi and Ganapathisubramani 2015). However, the effects of roughness-element configuration and the obstacle attributes were not considered (Kanda et al. 2013; Cheng and Porté-Agel 2015). Of course, most natural topographies exhibit large spatial heterogeneities, and mixing in the roughness sublayer is responsible for setting u_* and therefore the inertial layer momentum deficit (Xie et al. 2008; Napoli et al. 2008; De Marchis and Napoli 2012; Millward-Hopkins et al. 2013; Yuan and Piomelli 2014a; Giometto et al. 2016; Yang 2016). Recently, Kanda et al. (2013) proposed a refined z_0 model that is capable of incorporating the effects of spatial heterogeneity (Chung et al. 2015; Kondo et al. 2015; Krayenhoff et al. 2015). Kanda et al. (2013) found that the standard deviation of height σ_{h_o} (where the subscript implies standard deviation of the non-zero components of $h(x, y)$ only; see also Table 2) can well represent the effects of variation of, and the extreme value of, the building height through generalization of the original Macdonald et al. (1998) model, viz.,

$$\frac{z_0}{z_{0,\text{Mac}}} = b_1 Y^2 + c_1 Y + a_1,\tag{6}$$

where $Y = \lambda_p \sigma_{h_o}/\langle h_o \rangle$, $z_{0,\text{Mac}}$ is the roughness length from Eq. 5, and $a_1 = 0.71$, $b_1 = 20.21$, and $c_1 = -0.77$ are model parameters. Note that Table 2 contains a description of procedures used to compute statistic attributes of $h(x, y)$. The Macdonald et al. (1998) and Kanda et al. (2013) models performed well in terms of resolving the $\lambda_p - z_0/\langle h_o \rangle$ profile 'hump' and based on the correlation between actual and predicted values. However, they are contingent on a large number of empirical parameters. Thus, the problem of relating z_0 and geometrical roughness remains open, since local flow conditions may depend on details of the roughness elements in a highly case-specific fashion (Yang et al. 2016). In addition, we note that Eq. 6 is predicated on a statistical point of view, i.e. σ_{h_o}, which has been prominently used in the engineering roughness correlations. Herein we demonstrate that a generalized model based on statistical attributes can accurately predict z_0 for flow over complex urban-like topographies. Of course, for a given topography, knowledge of statistical attributes automatically implies that area indices (i.e. λ_p and λ_f) are known also (thus allowing use of Eqs. 5 and 6). The purpose of the present study is to propose an alternative modelling scheme that does not make use of area indices.

1.2 Engineering

In the engineering literature, equivalent sand-grain height, k_s, is typically used to represent surface roughness effects (that is, k_s is the engineering counterpart of z_0) (Jimenez 2004; Castro 2007). k_s has been the most commonly employed parameter to predict drag on rough surfaces (for a large parameter range, the Moody diagram provides estimated friction factor with changing inertial and roughness conditions k_s; Moody 1944; Nikuradse 1950; Yang et al. 2016). This parameter appears within the logarithmic law profile as (Allen et al. 2007),

$$\frac{U(z)}{u_*} = \frac{1}{\kappa} \ln\left(\frac{z}{k_s}\right) + B^*,\tag{7}$$

Table 2 Definitions of statistical parameters derived from topography, $h(x, y)$

Symbol	Description	Formulation
$\max(h)$	Maximum $h(x, y)$	$\max(h) = \underset{x,\, y}{\arg\max}(h(x, y))$
$\langle h \rangle$	Mean height of $h(x, y)$	$\langle h \rangle = \dfrac{1}{N_x N_y} \sum_{i=1}^{N_x} \sum_{j=1}^{N_y} h(x_i, y_j)$
$\langle h_o \rangle$	Mean height of blocks[a]	$\langle h_o \rangle = \dfrac{\sum_{i=1}^{N_x} \sum_{j=1}^{N_y} h(x_i, y_j)}{\sum_{i}^{N_x} \sum_{j}^{N_y} I(x_i, y_i)}$
σ_h	Standard deviation of $h(x, y)$	$\sigma_h = \left[\dfrac{1}{N_x N_y} \sum_{i=1}^{N_x} \sum_{j=1}^{N_y} (h(x_i, y_j) - \langle h \rangle)^2 \right]^{1/2}$
σ_{h_o}	Standard deviation of block heights	$\sigma_{h_o} = \left[\dfrac{\sum_{i=1}^{N_x} \sum_{j=1}^{N_y} I(x_i, y_i)(h(x_i, y_j) - \langle h_o \rangle)^2}{\sum_{i}^{N_x} \sum_{j}^{N_y} I(x_i, y_i)} \right]^{1/2}$
s_k	Skewness of $h(x, y)$	$s_k = \dfrac{\frac{1}{N_x N_y} \sum_{i=1}^{N_x} \sum_{j=1}^{N_y} (h(x_i, y_j) - \langle h \rangle)^3}{\left[\frac{1}{N_x N_y} \sum_{i=1}^{N_x} \sum_{j=1}^{N_y} (h(x_i, y_j) - \langle h \rangle)^2 \right]^{3/2}}$
k_u	Kurtosis of $h(x, y)$	$k_u = \dfrac{\frac{1}{N_x N_y} \sum_{i=1}^{N_x} \sum_{j=1}^{N_y} (h(x_i, y_j) - \langle h \rangle)^4}{\left[\frac{1}{N_x N_y} \sum_{i=1}^{N_x} \sum_{j=1}^{N_y} (h(x_i, y_j) - \langle h \rangle)^2 \right]^{2}}$

[a] Note that $I(x, y) = \mathcal{H}\left[h(x, y) - \delta_z/2 \right]$ is an indicator function, where $\mathcal{H}(x)$ is the Heaviside step function

where $B^* \approx 8.5$ is a model parameter. Note that Eqs. 1 and 7 can be combined to define the relationship between z_0 and k_s,

$$\frac{z_0}{k_s} = \exp\left(-\kappa B^* \right). \tag{8}$$

Various studies have investigated the effect of surface roughness on drag and attempted to develop a priori models for the prediction of k_s. This has paralleled more recent high-resolution numerical and experimental studies to explore the effects of complex roughness on wall turbulence (Wu and Christensen 2007, 2010; Mejia-Alvarez and Christensen 2010; Hong et al. 2011, 2012; Yuan and Piomelli 2014a, b, 2015; Anderson et al. 2015a; Chan et al. 2015). As in the boundary-layer meteorology community (see Sect. 1.1), the engineering community has developed models predicated on area ratios (Nikuradse 1950; Sigal and Danberg 1990; Rij et al. 2002; Flack and Schultz 2010). For complex roughness composed of more than one characteristic mode (i.e., the topography is the sum of a spectrum of topographic modes), statistical descriptions are appealing since a single geometric argument need not be defined. It has been common to scale z_0 linearly with the standard deviation of height, σ_h (see also Table 2),

$$\frac{z_0}{\sigma_h} = \alpha \tag{9}$$

where $\alpha \sim \mathcal{O}(10^{-1})$. For example, experimental measurements have indicated that $\alpha = 0.17$ (Hama 1954) and $\alpha = 0.1$ (Zagarola and Smits 1998; Shockling et al. 2006); for synthetic fractal landscapes wherein the radial energy spectrum of $h(x, y)$ exhibited a power-law

dependence with radial wavenumber, Anderson and Meneveau (2011) proposed a dynamic argument based on the Germano identity (Germano et al. 1991; Germano 1992) that dynamically predicted $\alpha \sim \mathcal{O}(10^{-1})$. More recently, however, it has been proposed that other statistical moments, i.e. skewness, s_k (see Table 2), should be used as a topographic moment upon which z_0 may scale. Notably, Flack and Schultz (2010) proposed,

$$\frac{z_0}{\sigma_h} = \alpha(1 + s_k)^\beta, \tag{10}$$

where $\alpha = 0.15$ and $\beta = 1.37$, while Ito et al. (2011) proposed,

$$\frac{z_0}{\sigma_h} = \alpha(1 + \beta s_k), \tag{11}$$

where $\alpha = 0.1$ and $\beta = 0.2$ for non-uniform roughness. The non-linear dependence of z_0 on s_k embodied in Eq. 10 is of particular importance to the present study, as will be seen below (note that Table 2 contains details of mathematical procedures used to compute statistical attributes derived from $h(x, y)$ and to generalize the Eq. 10 roughness correlation).

1.3 Present Study

A large-eddy simulation (LES) parametric study has been conducted on flows over synthetic, random, urban-like topographies. Compelled by the engineering roughness models (Sect. 1.2 and Eq. 10), we have systematically varied statistical moments of the topographies $- \sigma_h$, s_k, and kurtosis, k_u (see Table 2) – to explore the role of each on setting z_0 and d. That is,

$$z_0 = z_0(\sigma_h, s_k, k_u), \tag{12}$$

and,

$$d = d(\sigma_h, s_k, k_u). \tag{13}$$

Blocks are numerically resolved with an immersed boundary method, which enables a posteriori determination of z_0 and, thus, to evaluate the correlation of different statistical moments of the topography. Section 2 presents a brief summary of the LES code and description of the topographic arrangements considered, while Sect. 3 presents results of the simulations and numerical evaluation of roughness model parameters. In Sect. 4, we present results of a priori estimation of z_0 with a refined roughness correlation against predictions from other existing models; concluding remarks are provided in Sect. 5. The results demonstrate that z_0 can also be a priori correlated with statistical attributes of the topography, which serves as a complement to the existing body of knowledge on roughness models correlated with area indices.

2 Large-Eddy Simulation and Cases

2.1 Large-Eddy Simulation Code

The neutrally stratified, three-dimensional turbulent ABL is simulated using a LES model that has been used in a long series of ABL studies (Albertson and Parlange 1999; Porté-Agel et al. 2000; Bou-Zeid et al. 2005; Anderson and Meneveau 2010, 2011; Anderson 2012; Wilczek et al. 2015). The LES model solves the momentum transport equation for evolution of $\tilde{u}(x, t)$ under incompressible, $\nabla \cdot \tilde{u}(x, t) = 0$, and high Reynolds number, $\nu\nabla^2\tilde{u}(x, t) = 0$, conditions for $x \in \Omega$ and $t > 0$. Note that $\tilde{}$ denotes a grid-filtered (LES) quantity

(Meneveau and Katz 2000). Incompressibility is preserved by computing the divergence of the momentum transport equation, $\nabla \cdot \left[D\tilde{\boldsymbol{u}}/Dt = \nabla \cdot \boldsymbol{\sigma} \right]$, which yields a pressure Poisson equation that is solved for a pressure correction that preserves incompressible conditions.

The momentum transport equation is forced by an imposed streamwise pressure gradient (Eq. 2), which sets the friction velocity, u_*, upon which all velocities are scaled. Owing to spectral discretization in the horizontal directions, periodic boundary conditions are imposed on the vertical planes of the domain; channel centreline conditions are imposed with the zero-stress, $\partial \tilde{u}/\partial z = \partial \tilde{v}/\partial z$, and zero-penetration conditions, $\tilde{w} = 0$. Surface (i.e. $z/H = 0$) boundary conditions are implemented via the equilibrium logarithmic law and an immersed boundary method, depending on the value of $h(x, y)$. Where $h(x, y) = 0$ (i.e. 'no block' locations), stress is set as,

$$\tau_{xz}^w(x, y, t) = - \left[\frac{\kappa \, U(x, y, z, t)}{\ln\left(z/\hat{z}_0\right)} \right]^2 \frac{\overline{\tilde{u}}(x, y, z, t)}{U(x, y, z, t)}, \tag{14}$$

and,

$$\tau_{yz}^w(x, y, t) = - \left[\frac{\kappa \, U(x, y, z, t)}{\ln\left(z/\hat{z}_0\right)} \right]^2 \frac{\overline{\tilde{v}}(x, y, z, t)}{U(x, y, z, t)}, \tag{15}$$

where $\hat{z}_0/H = 1 \times 10^{-5}$ is a prescribed roughness length (summarized in Table 1), $\overline{\tilde{\cdot}}$ denotes test-filtering (Germano et al. 1991; Germano 1992), which is used here to suppress numerical contamination associated with localized implementation of Eqs. 14 and 15 (Bou-Zeid et al. 2005). Where $h(x, y) > 0$, an immersed boundary method is used (Anderson 2012) which has been successfully used in similar studies related to urban fluid mechanics (Anderson et al. 2015b; Anderson 2016). We emphasize that the prescribed $\hat{z}_0$ (used in Eqs. 14 and 15) is fundamentally different to the effective z_0 that will be computed a posteriori later based on the LES results. The small $\hat{z}_0$ value ensures that comparatively low drag is imposed due to the solid wall (where $h(x, y) = 0$). Subgrid-scale stresses are modelled with an eddy-viscosity model, $\boldsymbol{\tau}^d = -2\nu_t \boldsymbol{S}$, where $\boldsymbol{S} = \frac{1}{2}\left(\nabla \tilde{\boldsymbol{u}} + \nabla \tilde{\boldsymbol{u}}^{\mathrm{T}}\right)$ is the resolved strain-rate tensor. The eddy viscosity is $\nu_t = (C_s \Delta)^2 |\boldsymbol{S}|$, where $|\boldsymbol{S}| = (2\boldsymbol{S}{:}\boldsymbol{S})^{1/2}$, C_s is the Smagorinsky coefficient, and Δ is the grid resolution. For the present simulations, the Lagrangian scale-dependent dynamic model is used (Bou-Zeid et al. 2005).

2.2 Computational Set-Up

For all simulations, the domain $\boldsymbol{x} \in \Omega$ has spatial extents $\{(x, y, z) : 0 \le x \le 2H, 0 \le y \le 2H, 0 \le z \le H\}$, where H is the half-channel depth (here, $H = 1000$ m). The number of computational grid points, $N_x = N_y = N_z = 128$, with streamwise, spanwise, and vertical resolution, $\delta_x = 2H/N_x$, $\delta_y = 2H/N_y$, and $\delta_z = H/N_z$, respectively; the number of grid points per cube at each computational level depends on the number of cube spaces, N_c, in the array. In the present study, topographies were built with $N_c = 8$ or $N_c = 16$ in each direction and, thus, the number of grid points per cube is $N_x N_y / N_c^2 = 256$ or 64, respectively (please see Fig. 1 for visual inspection). However, as per Tables 3 and 4, $H/\max(h) \ge 3$, which ensures that the roughness sublayer and inertial layer are both resolved (Harmon and Finnigan 2007; Böhm et al. 2013; Anderson et al. 2015b). Similarly, the horizontal domain extent, $2H$, exceeds the streamwise integral length scale of the flow owing to vigorous mixing associated with the roughness sublayer (Kanda et al. 2004; Kanda 2006; Coceal et al. 2006, 2007; Xie et al. 2008). Simulations are run for at least $N_t \delta t U_0 u_* H^{-1} \sim \mathcal{O}(10^4)$ large-eddy turnovers,
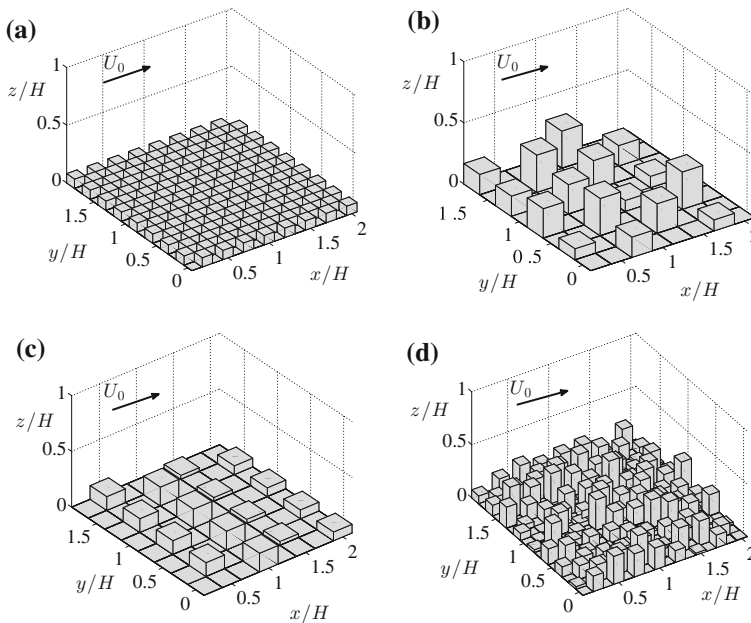
Fig. 1 Illustration of synthetic, urban-like topographies: Panel **a** shows the case 4 uniform arrangement; Panels **b**, **c** show irregular arrangements (cases 14 and 21, respectively); and Panel **d** shows the case 50 fully random arrangement. See Tables 3 and 4 for statistical details. Annotation, U_0, added to denote streamwise forcing direction

where $U_0 = \langle \tilde{u}(x, y, z/H = 1, t)\rangle_{xyt}$ (note that $\langle \dots \rangle_{xyt}$ denotes a plane- and time-averaged quantity), δt is the calculation timestep, and N_t is the total number of calculation timesteps.

2.3 Synthetic Urban-Like Topographies

We generated a suite of synthetic urban-like topographies with statistical attributes resembling real urban environments. For comprehensive details of how the topographies were constructed, please see Appendix. In order to systematically elucidate the effects of topographic statistical attributes (i.e. Eq. 12) on the mean flow and z_0, 56 topographies were built. Table 3 summarizes topographic statistical parameters used to determine z_0, and Fig. 1a–c illustrates select cases summarized in Table 3 (see caption for details). A range of staggered configurations is considered, which diversifies the range of topographic configurations upon which the model refinements are made. As a first effort, we have sought to determine the dependence of z_0 on individual statistical moments (Eq. 12), which is accomplished with cases 1–26. For these cases, one moment was varied while the remaining two were held constant (for example, consider cases 1–10, where σ_h is varied while s_k and k_u are held constant). This procedure forms the basis of establishing the hierarchical influence of σ_h, s_k, and k_u on setting z_0. Moreover, these results are used to broaden the range of topographic ensembles needed to inform roughness model parameters (recall Sect. 1.2 and Eq. 10). Cases 27–46 are used to investigate the effect of monotonically increasing roughness (evidenced by σ_h and s_k). As a final assessment of model efficacy, we considered cases 47–56, with attributes summarized in Table 4. These cases are unique since the block heights are randomly selected,

Table 3 Topographies used to determine z_0 and evaluate correlation parameters

Case	$\dfrac{\max(h)}{H}$	$\dfrac{\langle h_o \rangle}{H}$	$\dfrac{\langle h \rangle}{H}$	$\dfrac{\sigma_h}{H}$	$\dfrac{\sigma_h}{\langle h \rangle}$	s_k	k_u	$\dfrac{d}{H}$	$\dfrac{z_0}{H}$ [a]
1	0.020	0.020	0.010	**0.010**	1	*0*	*1*	0.020	1.938
2	0.040	0.040	0.020	**0.020**	1	*0*	*1*	0.038	3.852
3	0.050	0.050	0.025	**0.025**	1	*0*	*1*	0.045	4.080
4	0.060	0.060	0.030	**0.030**	1	*0*	*1*	0.055	4.903
5	0.080	0.080	0.040	**0.040**	1	*0*	*1*	0.075	6.190
6	0.100	0.100	0.050	**0.050**	1	*0*	*1*	0.085	6.627
7	0.120	0.120	0.060	**0.060**	1	*0*	*1*	0.105	8.498
8	0.150	0.150	0.075	**0.075**	1	*0*	*1*	0.133	9.772
9	0.200	0.200	0.100	**0.100**	1	*0*	*1*	0.170	12.423
10	0.250	0.250	0.125	**0.125**	1	*0*	*1*	0.215	14.785
11	0.318	0.208	0.052	*0.095*	1.838	**1.602**	*4.317*	0.195	21.963
12	0.308	0.203	0.051	*0.095*	1.875	**1.652**	*4.317*	0.190	22.491
13	0.310	0.202	0.051	*0.095*	1.890	**1.660**	*4.317*	0.190	23.877
14	0.304	0.200	0.050	*0.095*	1.908	**1.682**	*4.317*	0.170	24.868
15	0.280	0.197	0.049	*0.095*	1.936	**1.712**	*4.317*	0.165	25.294
16	0.300	0.189	0.047	*0.095*	2.024	**1.738**	*4.317*	0.162	24.962
17	0.290	0.188	0.047	*0.095*	2.035	**1.750**	*4.317*	0.162	26.834
18	0.277	0.182	0.045	*0.095*	2.100	**1.766**	*4.317*	0.148	28.696
19	0.163	0.100	0.010	*0.050*	2	*1.875*	**5.028**	0.090	11.935
20	0.166	0.100	0.025	*0.050*	2	*1.875*	**5.069**	0.085	12.415
21	0.167	0.100	0.025	*0.050*	2	*1.875*	**5.098**	0.075	12.304
22	0.168	0.100	0.025	*0.050*	2	*1.875*	**5.118**	0.080	12.515
23	0.169	0.100	0.025	*0.050*	2	*1.875*	**5.132**	0.090	11.581
24	0.169	0.100	0.025	*0.050*	2	*1.875*	**5.143**	0.070	13.127
25	0.169	0.100	0.025	*0.050*	2	*1.875*	**5.151**	0.090	11.780
26	0.170	0.100	0.025	*0.050*	2	*1.875*	**5.161**	0.075	12.730
27	0.060	0.048	0.024	*0.025*	1.067	**0.342**	**1.442**	0.045	4.305
28	0.063	0.048	0.024	*0.026*	1.101	**0.478**	**1.610**	0.052	4.656
29	0.066	0.043	0.022	*0.027*	1.254	**0.871**	**2.058**	0.054	4.565
30	0.067	0.041	0.021	*0.028*	1.343	**0.996**	**2.187**	0.052	4.717
31	0.115	0.098	0.049	*0.050*	1.032	**0.176**	**1.231**	0.088	7.748
32	0.125	0.093	0.046	*0.052*	1.117	**0.532**	**1.674**	0.091	8.493
33	0.128	0.084	0.042	*0.052*	1.245	**0.854**	**2.041**	0.091	10.479
34	0.130	0.075	0.038	*0.054*	1.441	**1.079**	**2.267**	0.095	10.602
35	0.175	0.148	0.074	*0.076*	1.034	**0.189**	**1.247**	0.135	13.807
36	0.185	0.133	0.066	*0.076*	1.146	**0.625**	**1.785**	0.138	16.554
37	0.185	0.113	0.056	*0.076*	1.353	**1.006**	**2.197**	0.133	17.605
38	0.185	0.185	0.046	*0.080*	1.732	**1.155**	**2.333**	0.125	18.066
39	0.230	0.195	0.098	*0.100*	1.032	**0.176**	**1.231**	0.178	17.595
40	0.240	0.185	0.093	*0.100*	1.085	**0.415**	**1.533**	0.180	20.958
41	0.250	0.155	0.078	*0.103*	1.323	**0.973**	**2.164**	0.175	24.330

Table 3 continued

Case	$\dfrac{\max(h)}{H}$	$\dfrac{\langle h_o \rangle}{H}$	$\dfrac{\langle h \rangle}{H}$	$\dfrac{\sigma_h}{H}$	$\dfrac{\sigma_h}{\langle h \rangle}$	s_k	k_u	$\dfrac{d}{H}$	$\dfrac{z_0}{H}$ [a]
42	0.251	0.146	0.073	*0.104*	1.432	**1.074**	**2.262**	0.180	24.246
43	0.290	0.245	0.123	*0.126*	1.033	**0.184**	**1.241**	0.220	25.000
44	0.310	0.230	0.115	*0.128*	1.114	**0.525**	**1.665**	0.230	26.419
45	0.320	0.210	0.105	*0.131*	1.245	**0.854**	**2.041**	0.230	28.583
46	0.320	0.185	0.093	*0.132*	1.437	**1.077**	**2.265**	0.230	29.149

Bold relief has been used to highlight the statistical moment being varied. Italic relief has been used to highlight the statistical moment that remains fixed. See Table 2 for definition of statistical parameters
[a] Value has been multiplied by 10^3 for discussion

Table 4 Topographies used for validation of applicability of the correlation for fully random cases

Case #	$\dfrac{\langle h \rangle}{H}$	$\dfrac{\sigma_h}{H}$	$\dfrac{\sigma_h}{\langle h \rangle}$	s_k	k_u	$\dfrac{d}{H}$	$\left.\dfrac{z_0}{H}\right|_A^a$	$\left.\dfrac{z_0}{H}\right|_P^a$	% Diff.
47	0.022	0.030	1.354	1.006	2.880	0.063	6.544	7.755	18.5
48	0.043	0.060	1.408	1.140	2.839	0.115	15.512	15.613	0.7
49	0.056	0.069	1.229	0.741	1.963	0.135	14.147	14.612	3.3
50	0.069	0.090	1.309	1.006	2.644	0.188	24.746	21.907	−11.5
51	0.078	0.100	1.288	0.890	2.240	0.205	21.066	23.030	9.3
52	0.058	0.071	1.225	0.839	2.466	0.153	16.117	15.864	−1.6
53	0.071	0.085	1.202	0.836	2.550	0.178	21.451	19.083	−11.0
54	0.097	0.110	1.142	0.559	1.869	0.223	22.788	21.210	−6.9
55	0.122	0.140	1.149	0.653	2.158	0.285	37.856	28.379	−25.0
56	0.123	0.150	1.220	0.843	2.484	0.295	45.999	33.723	−26.7

Here, $\left.\dfrac{z_0}{H}\right|_A^a$ stands for the roughness lengths obtained a posteriori from LES, and $\left.\dfrac{z_0}{H}\right|_P^a$ stands for a priori from empirical correlations (Eq. 26). See Table 2 for definition of statistical parameters
[a] Value has been multiplied by 10^3 for discussion

which thus can represent the heterogeneity and randomness of real urban geometry. Figure 1d illustrates case 50, which exhibits substantial spatial heterogeneity.

3 Roughness Correlations and Geometric Statistics

3.1 A Posteriori Determination of z_0 from Mean Streamwise Velocity Component

Mathematically, z_0 is defined as the elevation at which the mean streamwise velocity component is zero (recall Sect. 1 and Eq. 1). This definition is complicated for the current cases owing to the presence of a dramatic canopy of obstacles that collectively induce the inflected roughness sublayer $\langle \tilde{u}(z) \rangle_{xyt}$ profile and vertically displacing the elevation at which $\langle \tilde{u}(z) \rangle_{xyt}$ exhibits a logarithmic form (Raupach et al. 1991, 1996; Coceal et al. 2006; Yang et al. 2016). In Eq. 1, the length $(z - d)$ is a corrected elevation based on the zero-plane displacement, d, which is introduced to collapse the logarithmic mean streamwise velocity component profile
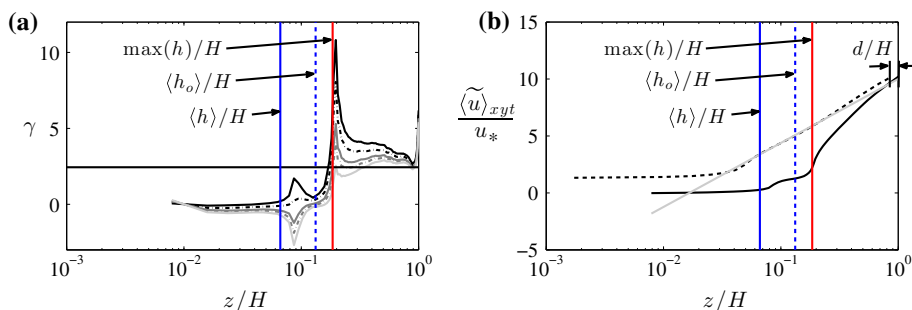
Fig. 2 (Colour) Statistics of the mean streamwise velocity component for case 36. Panel **a** shows γ (Eq. 16) against elevation for $\gamma = \kappa^{-1}$ (*solid black horizontal line*), $d/H = 0.04$ (*solid black line*), $d/H = 0.08$ (*dash-dotted black line*), $d/H = 0.12$ (*solid dark grey line*), $d/H = 0.138$ (*dashed dark grey line*), and $d/H = 0.16$ (*solid light grey line*). Panel **b** shows mean streamwise velocity component profiles: original profile from LES (*solid black line*), d-compensated velocity profile (*dashed black line*), and logarithmic profile (*solid grey line*). For reference, both figures include vertical profiles for $\langle h \rangle / H$ (*vertical solid blue line*), $\langle h_o \rangle / H$ (*vertical dashed blue line*), and $\max(h)/H$ (*vertical solid red line*)

(Su et al. 2008). With this definition, z_0 retains its definition as $\langle \tilde{u}(z_0) \rangle_{xyt} = 0$. For the present purposes, we evaluate d using the 'second method' (Cheng and Castro 2002; Coceal et al. 2006), which then enables computation of z_0. This is accomplished via computation of the vertical gradient of the Eq. 1 profile, $d\langle \tilde{u}(z) \rangle_{xyt}/dz$ (Moser et al. 1999). In doing so, z_0 vanishes since it is a constant and the gradient can be rearranged to obtain,

$$\gamma = \frac{z - d}{u_*} \frac{d\langle \tilde{u}(z) \rangle_{xyt}}{dz} = \frac{1}{\kappa}. \tag{16}$$

We evaluate d based on best-fit agreement with the inertial layer logarithmic profile, since each d yields a unique $\gamma = \kappa^{-1}$. This was accomplished with an iterative approach, where each successive value of d yields a cumulative error against the logarithmic profile and the value associated with the smallest error was selected. This is graphically illustrated in Fig. 2a, where the solid black horizontal line corresponds with $\gamma = \kappa^{-1} = 2.5$, while other lines correspond with different d from a LES dataset. For this particular case (case 36), the resulting displacement height was $d/H = 0.138$, $d/\langle h_o \rangle = 0.138/0.1325 \approx 1.04$, and $d/\max(h) = 0.138/0.185 \approx 0.75$. This result is supported by experimental data from Hagishima et al. (2009) and Zaki et al. (2011), who demonstrated that d for complex urban-like topographies (variable height, spatial staggering) can exceed $\langle h_o \rangle$.

The effect of the zero-plane displacement d can be better explained in Fig. 2b. The solid black line corresponds with the original profile from the LES dataset, the dashed black line is the LES profile plotted against $(z - d)/H$, and the solid grey line is the logarithmic profile (i.e. Eq. 1). Prior to introduction of d, the slope of the $\langle \tilde{u}(z) \rangle_{xyt}$ profile differs from the logarithmic profile. With an appropriate d, $\langle \tilde{u}(z) \rangle_{xyt}$ collapses to the logarithmic profile. At this stage, the logarithmic profile can be extrapolated to the elevation for $\langle \tilde{u}(z) \rangle_{xyt} = 0$, which is $z/H = z_0/H$. Included in this figure are vertical profiles representing salient geometric attributes of the topography ($\langle h \rangle / H$, $\langle h_o \rangle / H$, and $\max(h)/H$), which is illuminating for relating the $\langle \tilde{u}(z) \rangle_{xyt}$ inflection to block height (Coceal et al. 2006; Ghisalberti 2009; Anderson et al. 2015b). Since $3 \lesssim z_{RSL}/\langle h_0 \rangle \lesssim 5$ (recall Sec. 1), and because $\langle h_0 \rangle / H = 0.133$ for Fig. 2b case, we can estimate that $0.4 \lesssim z_{RSL}/H \lesssim 0.665$. These approximate depths provide guidance on the region of the flow that should be expected to exhibit logarithmic scaling, and close inspection of Fig. 2b shows relatively close agreement with the logarithmic profile for
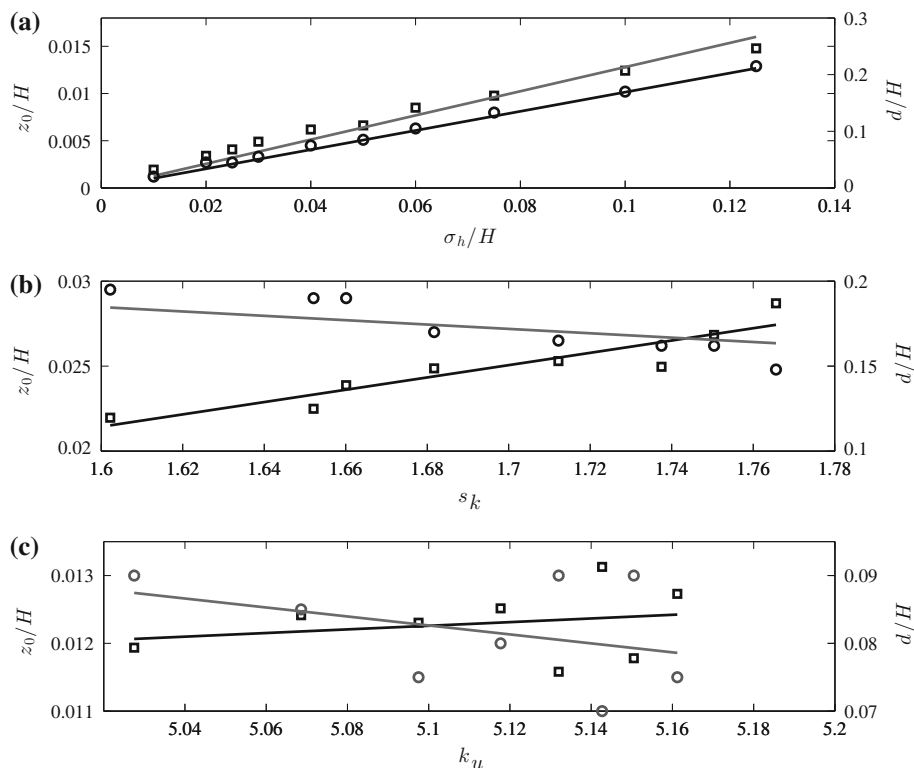
Fig. 3 Parametric evaluation of the sensitivity of z_0 and d to different statistical moments of the topography. Panel **a** shows z_0/H and d/H with respect to σ_h/H (cases 1–10; Table 3); Panel **b** shows z_0/H and d/H with respect to s_k (cases 11–18; Table 3), and Panel **c** shows z_0/H and d/H with respect to k_u (cases 19–26; Table 3). The left- and right-side ordinate on panels **a**–**c** shows the value of z_0/H and d/H, respectively. *Open squares* and *circles* correspond with z_0/H and d/H, respectively. In all figures, *open symbols* correspond with individual LES cases while solid profiles are error-minimized fitted profiles (*black* and *grey* correspond with z_0/H and d/H, respectively)

$z/H \gtrsim 0.7$. There is slight departure from the logarithmic profile that would diminish with longer simulations, but for the present purposes of determining bulk aerodynamic parameters with such an extensive numerical campaign, this level of agreement is satisfactory.

3.2 Hierarchy of Topography Statistical Moments

We have used the Sect. 3.1 approach to determine z_0 and d for cases 1–26, summarized in Table 3. For the urban-like topographies considered, this approach enables clear evaluation of the extent to which aerodynamic properties depend on different topographic statistical moments (σ_h, s_k, and k_u). The results are also used to establish the hierarchical importance of these moments. Figure 3a–c, show how z_0 and d vary with respect to σ_h, s_k, and k_u, respectively. From inspection, we immediately discern that there is a declining dependence with increasing moment, from a very strong linear scaling on σ_h to an essentially negligible scaling with k_u. It is emphasized that the vertical range of values for z_0 (left ordinate) and d (right ordinate) decreases monotonically from Fig. 3a–c: if the same vertical range of values had been adopted for all figures, the diminishing influence of higher order moments

Table 5 Summary of the dependence of z_0 and d with topographic moments based on cases 1–26

Gradient	R^2
$\dfrac{\partial z_0}{\partial \sigma_h} = 0.128$	0.961
$\dfrac{\partial d}{\partial \sigma_h} = 1.690$	0.993
$\dfrac{\partial (z_0/H)}{\partial s_k} = 0.036$	0.872
$\dfrac{\partial (d/H)}{\partial s_k} = 0.128$	0.674
$\dfrac{\partial (z_0/H)}{\partial k_u} = 0.003$	0.175
$\dfrac{\partial (d/H)}{\partial k_u} = 0.066$	0.039

would have been further highlighted. In fact, we have computed the slope of the error-minimized fitted profiles in Fig. 3 and the resultant coefficient of determination, $R^2 = 1 - \Sigma_i (y_i - f_i)^2 / \Sigma_i (y_i - \overline{y})^2$, where y_i represent individual datapoints from simulations and f_i is the model fit. These values are summarized in Table 5.

Table 5 gradients and R^2 values demonstrate the diminishing dependence of z_0 and d on higher-order moments. In all cases of strong statistical dependence (i.e., for $R^2 \gtrsim 0.7$), Fig. 3 indicates a linear scaling of roughness parameter on topographic moment. Interestingly, we note that the gradient, $\partial z_0/\partial \sigma_h \approx 0.1$, is almost equivalent to the $z_0 - \sigma_h$ scaling and constant of proportionality, $\alpha \approx 0.1$, in Eq. 9 (and accompanying discussion). Thus, $\alpha \approx 0.1$ appears to be valid for diverse urban-like topographic arrangements. From the Table 5 results, we contend that k_u can be neglected with no loss of generality and, thus, Eq. 12 reduces to,

$$z_0 = z_0(\sigma_h, s_k) = f(\sigma_h)g(s_k) = \alpha\sigma_h g(s_k), \tag{17}$$

where the function, $g(s_k)$ incorporates the effects of skewness ($g(s_k) = 1$ for $s_k = 0$) (Flack and Schultz 2010; Ito et al. 2011). Moreover, these results demonstrate that Eq. 13 can be reduced to,

$$d = d(\sigma_h) = \alpha_d \sigma_h, \tag{18}$$

where $\alpha_d = 1.69$; this dimensional dependence is predicated on the declining gradient and the values of R^2 (note that this relation exhibits the highest R^2). It is noted also that $\alpha_d = 1.69$ is almost identical to the constant of proportionality used by Theurer (1993) to correlate d with $\lambda_p \langle h_0 \rangle$ (see also Table 1). In order to validate claims regarding the reduced dimensional dependence argued in this section (i.e. from Eqs. 12 and 13 to Eqs. 17 and 18, respectively), we have performed a variance-based sensitivity analysis (VBSA; Saltelli et al. 2000, 2010). By using VBSA, one can quantify the sensitivity of model output (z_0 and d) to the constituent inputs (in this work, we claim that σ_h, s_k, and k_u are the attributes that set aerodynamic parameters, although subsequent results will illustrate that resultant prognostic models exhibit errors that is inherent to the use of empirical relations; see Sect. 4 and Figs. 6 and 7). VBSA is ideally suited to the present application, where one constituent input has been varied while the remaining two were fixed. The use of VBSA is predicated upon decomposition of the variance per input,

$$\sigma_{\mathcal{Y}}^2 = \sum_{i=1}^{n} \sigma_i^2 + \sum_{i<j}^{n} \sigma_{ij}^2 + \cdots + \sigma_{12\ldots n}^2, \tag{19}$$

where we have introduced the model, $\mathcal{Y} = f(X)$, for generality. The definition for variance is shown in Table 2. VBSA can be used to determine the sensitivity of $\mathcal{Y}$ to variation of an individual input, X_i, or to simultaneous variation of multiple inputs, $X_{ij\ldots n}$, which implies the existence of n inputs for model, $\mathcal{Y} = f(X)$; given the nature of this study, we have truncated Eq. 19 to consider only the variation of individual inputs. The method culminates in a non-dimensional sensitivity index for each input, i, expressed as,

$$S_i = \frac{\sigma_i^2}{\sigma_{\mathcal{Y}}^2}. \tag{20}$$

S_i is a proper measure of sensitivity to input variability and an appropriate tool for establishing input parameter hierarchy, even if the model is non-additive and the input factors are correlated (Ratto et al. 2001; Mara and Tarantola 2012). For $\mathcal{Y} = z_0$ and d, we have used cases 1–10, 11–18, and 19–26 to determine the sensitivity to σ_h, s_k, and k_u, respectively. The resulting sensitivity indices are shown in Fig. 4, which clearly highlights the diminishing influence of higher-order moments. Figure 4a shows that z_0 is sensitive to both σ_h and s_k, while Fig. 4b shows that d is predominantly affected by variations in σ_h. Two matters related to this analysis are emphasized:

i. A natural consequence of VBSA, wherein constituent variances are computed and measured against the total, is that the sum of all sensitivity indices is unity,

$$\sum_{i=1}^{n} S_i + \sum_{i<j}^{n} S_{ij} + \cdots + S_{12\ldots n} = 1. \tag{21}$$

Here we hypothesize that, to reasonably good approximation, z_0 scales with σ_h and s_k and d scales with σ_h. Of course, this approach is tantamount to homogenizing aerodynamically-relevant spatial details of the topography into statistical moments, and z_0 and d will also be affected by other details. Indeed, the arguments presented in Eqs. 12 and 13 could have been further generalized to reflect the potential dependence on the nth moment, $\langle (h - \langle h \rangle)^n \rangle$, but the preceding literature suggests that such generality is not needed (Flack and Schultz 2010). This is reflected in the values of S_i shown in Fig. 4, and in the deviations between actual and predicted z_0 (discussion to follow in Sect. 4). Nonetheless, the values for S_i show that z_0 and d are strongly influenced by statistical moments of the topography.

ii. Figure 4b shows that $\sum_{i=1}^{3} S_i > 1$ for the application of VBSA to sensitivity analysis of d. VBSA is typically applied to datasets with a larger number of samples (Saltelli 2002), and it is anticipated than an even larger parametric study, would correct this.

Having now established that k_u can be neglected in models for z_0, and given the overwhelmingly comprehensive evidence that $\alpha \approx 0.1$, we seek next to explore the influence of skewness. Though recent models have proposed inclusion of s_k (Flack and Schultz 2010; Ito et al. 2011), the applications have been for roughness Reynolds number conditions, $Re_* = u_* H / \nu$, less than the present 'asymptotic' ABL conditions. Similarly, to our knowledge, the application of such models (i.e. Eqs. 10, 11) to ABL and urban-flow processes has not been explored. It should be emphasized that Eqs. 12–17 reduction (i.e. claiming that z_0 does not scale with k_u) is based on a relatively narrow range of k_u values. It is difficult to build a set of distinctly different topographies with variable k_u but constant s_k and σ_h, and
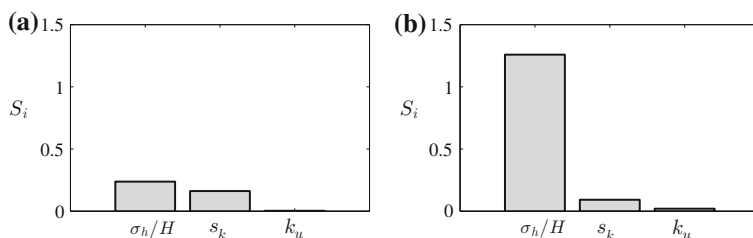
Fig. 4 Results of variance-based sensitivity analysis, applied to the cases 1–26 datasets summarized in Table 3. The *panels* show sensitivity of z_0 (Panel **a**) and d (Panel **b**) to variation of σ_h, s_k, and k_u

the range considered here represents the author's best attempts to evaluate the influence of k_u. But, it is entirely possible that the z_0 dependence on k_u may be present for values not considered here.

3.3 Effects of Skewness (s_k)

In order to generalize the results and educe the role of skewness, we have considered cases 27–46 (attributes summarized in Table 3). These cases are important since they embody the more realistic features of urban environments in which σ_h may exhibit small variability and not detect 'outlier' elements (i.e. tall buildings that s_k would capture). Given the multiplicative nature of Eq. 17 (between the functions $f(\sigma_h)$ and $g(s_k)$), we need now to evaluate $g(s_k)$. Since $f(\sigma_h) = \alpha\sigma_h$ and because $g(s_k)$ is a dimensionless factor, we adopt the following approach

$$g(s_k) = \frac{z_0(\sigma_h, s_k)}{z_0(\sigma_h, s_k = 0)}, \tag{22}$$

when $\sigma_h/H = $ constant, where, as noted, $g(s_k = 0) = 1$. Thus, Eq. 22 reveals the functional dependence of $g(s_k)$ on s_k; put differently, $g(s_k) = 1$ for no functional dependence, indicating that 'outlier' buildings extract negligible momentum from the flow. Figure 5a shows $g(s_k)$ with respect to s_k, which firstly indicates that $g(s_k)$ (and, by extension, z_0) is influenced by s_k. Moreover, staggering between the $g(s_k)$ profiles indicates that the function is itself dependent on σ_h (discussion to follow), i.e.

$$g(s_k) = g(\sigma_h, s_k). \tag{23}$$

Finally, we note that s_k appears to have a diminishing influence on the function $g(s_k)$, and that $g(\sigma_h, s_k) \rightarrow g(\sigma_h)$ for $s_k \gtrsim 1$. We stress also that, while H is the ABL depth and, therefore, not a topographic attribute, it is an acceptable normalizing scale for Fig. 5a since the same value is used for all cases.

In the comprehensive experimental measurements by Flack and Schultz (2010), they proposed the following model for skewness effects (Eq. 17),

$$g(s_k) = (1 + s_k)^\beta, \tag{24}$$

where the exponent, $\beta = 1.37$. For the range of topographies considered here, we have computed the resultant β from Eq. 24. This has been accomplished a posteriori using results from the LES cases. Specifically, we evaluate β for each $s_k - g(s_k)$ data point in Fig. 5a, $\beta = \ln[g(s_k)]/\ln(1 + s_k)$, with the resultant values shown on Fig. 5b. We show the resultant β values against $\sigma_h/\langle h \rangle$ (instead of σ_h/H), which ensures that the length is normalized by a static topographic attribute. Figure 5b shows that $\beta = \beta(\sigma_h/\langle h \rangle)$ for $\sigma_h/\langle h \rangle \lesssim 1.15$, while
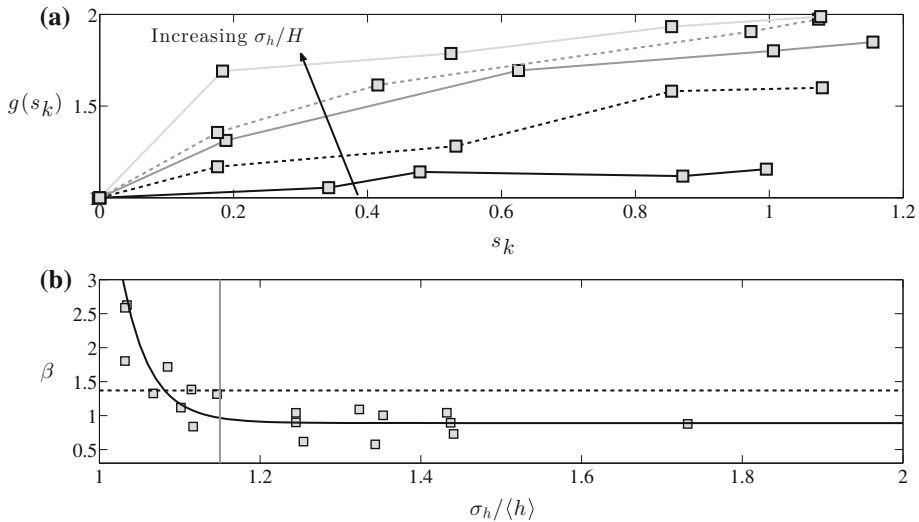
Fig. 5 Evaluation of function $g(s_k)$. Panel **a** shows the functional dependence of $g(s_k)$ on s_k (i.e. Eq. 22). *Individual symbols* correspond to results from LES cases 27–46, while *solid lines* are added between cases to 'connect' constant σ_h cases. *Solid black line*, $\sigma_h/H = 0.025$ (cases 27–30); *dashed black line*, $\sigma_h/H = 0.05$ (cases 31–34); *dash-dotted black line*, $\sigma_h/H = 0.075$ (cases 35–38); *solid grey line*, $\sigma_h/H = 0.1$ (cases 39–42); *dashed grey line*, $d/H = 0.125$ (cases 43–46). See Table 3 for comprehensive details of topographies. Panel **b** shows the functional dependence of $\beta = \ln\left[g(s_k)\right]/\ln(1+s_k)$ on $\sigma_h/\langle h \rangle$ using panel (**a**) data, where *individual symbols* correspond with constant-σ_h profiles. *Solid black line* is error-minimized fitted profile to LES datapoints; *dashed black line* is $\beta = 1.37$ (Flack and Schultz 2010)

$\beta \approx 0.9$ for $\sigma_h/\langle h \rangle \gtrsim 1.2$. This is close to the value reported by Flack and Schultz (2010), who suggest $\beta = 1.37$; it is certainly possible also that deviations in the prescribed α could alter the resultant β (Eq. 17). But since β does not exhibit a constant value, a generalized version of the Flack and Schultz (2010) model cannot be used for the entire range of $\sigma_h/\langle h \rangle$. We have found, however, that a generalized version of the Ito et al. (2011) model can be used to close the system for $\sigma_h/\langle h \rangle \lesssim 1.15$. In this sense, the refined model is a "hybrid" combination of both approaches, with model parameters tuned for atmospheric flows over urban-like topographies. We propose the following generalized approach to the closure of Eq. 23,

$$g(\sigma_h/\langle h \rangle, s_k) = \begin{cases} 1 + \beta s_k, & \sigma_h/\langle h \rangle < 1.15 \\ (1+s_k)^\beta, & \sigma_h/\langle h \rangle \geq 1.15, \end{cases} \tag{25}$$

where $\beta = 0.9$. Substitution of Eq. 25 into Eq. 17 yields the final roughness correlation,

$$z_0(\sigma_h, s_k) = \begin{cases} \alpha\sigma_h(1 + \beta s_k), & \sigma_h/\langle h \rangle < 1.15 \\ \alpha\sigma_h(1+s_k)^\beta, & \sigma_h/\langle h \rangle \geq 1.15. \end{cases} \tag{26}$$

Below, the efficacy of Eq. 26 as a prognostic correlation is tested against existing models, experimental datasets, and a posteriori z_0 values for cases 47–56 in Table 4.

4 Model Comparison

In order to assess the performance of Eq. 26 in a quantitative manner, we wish to compare predictions from Eq. 26 with existing roughness models (see Sect. 1.1 and Table 1). Many of these models are predicated upon packing density, λ_p, which indicates that the roughness length increases in the sparse regime, and then decreases after the peak for increased values of solidity (this is principally related to the transition from k-type roughness to d-type roughness and the effects of sheltering from adjacent elements: see Perry et al. 1969; Macdonald et al. 1998; Leonardi et al. 2003; Jimenez 2004; Cheng et al. 2007; Coceal et al. 2007; Hagishima et al. 2009; Leonardi and Castro 2010; Kanda et al. 2013; Placidi and Ganapathisubramani 2015). Here, we note that Yang et al. (2016) recently developed a self-contained roughness sublayer model that dynamically embodies the effects of sheltering and thus predicts the effects of spacing on surface momentum fluxes for sparse and dense canopies. We wish to demonstrate that Eq. 26 captures the bulk effects of sheltering (inherent to complex urban topographies) without the explicit use of λ_p. The results and generalized model presented here, which are solely based on statistical moments of $h(x, y)$, do not use parameter λ_p, but the empirical parameters are informed by comprehensive numerical simulations that capture sheltering effects.

Performance against existing models is quantified by considering topographies composed of cubic elements. In this approach, we have adopted the topographic "stencil" used in Cheng and Castro (2002), Coceal et al. (2006), and Leonardi and Castro (2010), and varied λ_p by changing the side-length of cubic elements. For each λ_p, we compute all the Eq. 26 input arguments, σ_h, $\sigma_h/\langle h \rangle$, and s_k, and then compute $z_0/\langle h_0 \rangle$. Figure 6 shows the results of inter-comparison between the different roughness models with λ_p, and several experimental datasets (see accompanying caption for additional details). Here, Eq. 26 is tested for $0.05 \leq \lambda_p \leq 0.5$ (we also test the constant-β model introduced by Flack and Schultz 2010 in an identical fashion). The model has not been applied to $\lambda_p < 0.05$ since, aerodynamically, such a value is indicative of sparseness resembling an isolated element affixed to a flat wall, rather than an urban environment composed of a distribution of elements (Macdonald et al. 1998).

It is apparent that existing models considered for Fig. 6 predict the z_0 'hump' associated with the k-to-d-type roughness transition for $0.2 \lesssim \lambda_p \lesssim 0.4$. Moreover, it is clear that the Eq. 24 model for $g(s_k)$ with $\beta = 1.37$ overpredicts z_0 for relatively small λ_p, while Eq. 26 exhibits much stronger agreement with published datasets and existing models (including an evident change of slope for $\lambda_p \approx 0.2$). We also emphasize that all the roughness models exhibit a similar trend of declining z_0 with increasing λ_p for $\lambda_p \gtrsim 0.3$. One can see also that predicted values of z_0 are most sensitive to modelling approaches for smaller (more sparse) λ_p. For the test case of urban-like topographies composed of cubic elements, Eq. 26 predictions compare favourably with datasets from experimental measurements and direct numerical simulation and large-eddy simulation.

Figure 6 shows that the Eq. 26 model works well for the present geometries, and we wish to test its applicability for fully irregular cases. For this purpose, we consider cases 47–56, as summarized in Table 4 (see also Fig. 1d for case 50 as an example). These complex, random topographies possess attributes that resemble real urban environments. For these cases, Fig. 7 shows the comparison of roughness lengths attained a posteriori from LES, and a priori from empirical correlations (Eq. 26; the Macdonald et al. 1998 model; and the Kanda et al. 2013 model). For illustration, a one-to-one linear profile (solid black) was added, which provides a visual basis on the level agreement between actual and predicted values. For validation results
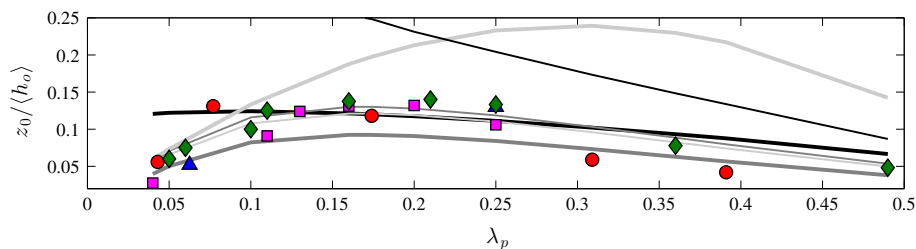
Fig. 6 (Colour) Variation of roughness length against λ_p, relevant to Eq. 26 with respect to packing density, λ_p (Eq. 4) for the cubical cases ($\lambda_p \equiv \lambda_f$). Solid profiles correspond with: Eq. 26 (*thick black line*); Eq. 24 with $\beta = 1.37$ (Flack and Schultz 2010) (*thin black line*); Theurer (1993) model (*thick light grey line*); Kanda et al. (2013) Model # 1 (*thin dark grey line*); Kanda et al. (2013) Model # 2 (*thick dark grey line*); Macdonald et al. (1998) model (*thin dark grey line*). *Symbols* correspond with: Hagishima et al. (2009) experiments (*red circle*); Cheng et al. (2007) experiments (*blue triangle*); Leonardi and Castro (2010) direct numerical simulations (*pink square*); Kanda et al. (2013) LES (*green diamond*)
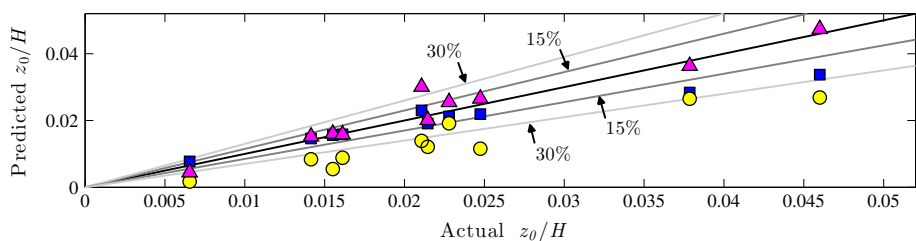
Fig. 7 (Colour) Comparison of z_0 (for cases 47–56) attained a posteriori from LES (actual z_0/H), and a priori from empirical correlations (predicted z_0/H). *Solid black line* indicates 1:1. *Blue squares* indicate Eq. 26, *yellow circles* Macdonald et al. (1998) model, *pink triangles* Kanda et al. (2013) model

of the present numerical treatment for urban-like topographies, see Anderson et al. (2015b). It is clear that for the urban-like geometry with variable height, the Macdonald et al. (1998) model underestimates z_0 since it does not account for geometric variability. Meanwhile, we note that the Eq. 26 model and Kanda et al. (2013) model compares favourably against LES results. As the Kanda et al. (2013) model is the modified Macdonald et al. (1998) model when the obstacles exhibits randomly varying height, the result of the present study further proves that for irregular geometry, the variability of urban surface height has an important impact on the bulk roughness parameters.

5 Conclusion

Statistical moments of the surface height are used to represent the heterogeneity and randomness of complex, urban-like geometries. Owing to the inherent non-linearity and spatial complexity associated with turbulent flow in urban canopies, we have used an extensive parametric study to educe the hierarchical influence of increasing statistical moments. As has already been well established, the roughness length exhibits a linear scaling on standard deviation. However, skewness and kurtosis (as measures of the presence of extreme value, 'heavy tail' events) have received somewhat less attention topographic parameters for modelling z_0. Results presented here show that skewness and kurtosis exhibit a diminishing influence on z_0, and we conclude that z_0 has a negligible dependence on kurtosis.

Skewness, on the other hand, has a non-negligible influence, which prompted consultation of a novel roughness parameterization recently proposed by Flack and Schultz (2010). We adopt their model, but find that further generalization is needed for applications to urban-like topographies. We show that the generalized model performs well against existing models and captures the increasing-decreasing roughness form due to the k-to-d-type roughness transition (Jimenez 2004). It would be of interest to compare predictions from the generalized Flack and Schultz (2010) model for real urban environments, as was recently done by Ratti et al. (2002) and Kanda et al. (2013), but their models do not include any higher statistical moment, i.e. skewness. Nonetheless, we once more cite Figs. 6 and 7 results as evidence that the present statistics-based model performs well for simplified model geometries and urban-like distributions. With these results, we propose use of an alternative scheme that does not rely on area indices.

The topographies considered herein (Tables 3, 4) were composed of staggered distributions of square-based prisms. The spacing between adjacent prisms was set by the base geometry, where adjacent prisms where either in contact or spaced by the cube side length. Real urban topographies are composed of prism-like geometries that are neither square-based nor spaced evenly. Instead, their spatial extent (in $x - y$) varies (where a rectangular shape is the exception), as do the spacing between adjacent elements. Such complexity is beyond the scope of the present work. We contend, however, that the model performance observed here (Figs. 6, 7) is strong, and the approach is itself grounded in mechanical engineering applications to complex (heterogeneous) roughness. Therefore, since the input arguments, σ_h and s_k, embody the effects of such spatial heterogeneity, we anticipate that Eq. 26 would perform well with realistic topographies. But only experimental measurements or additional simulations can fully substantiate this claim. Here, we also note recent work that has addressed the topic of spatial heterogeneity of urban environments and aerodynamic signature. Yang et al. (2016) and Yang (2016) developed numerical treatments specifically for the purpose of variable spacing between adjacent elements, while Giometto et al. (2016) recently studied the turbulence structure above an actual urban environment.

Roughness models impose a momentum deficit due to z_0 and u_* (Eq. 1), and thus induce a shift in the logarithmic profile but assume it remains logarithmic to $z = z_0$. They, of course, do not include the *actual* processes occurring in the canopy and roughness sublayer that are responsible for setting u_* (vigorous, mixing-layer-like processes, see Ghisalberti 2009). Nonetheless, the present scheme may find utility for initializing high-resolution LES or for numerical weather prediction at regional scales.

Appendix: Topography Construction

The topographies summarized in Tables 3 and 4 were built in MatLab$^{\text{TM}}$. Construction of the topographies involved designation of two topographic "stencils", where block heights are either fixed to zero or are allowed to vary at pre-defined locations. For cases 1–10, a topographic stencil with 256 uniform-height, square-based blocks was distributed across the $N_x = N_y = 128$ computational grid (i.e., each block had side length, $L_x/16$; see also Fig. 1a). The height of the blocks was varied as $0.02 \leq h_o/H \leq 0.25$, and thus the standard

deviation, σ_h/H, was changed systematically while the skewness and kurtosis were set to fixed values (recall the description of topographic moments in Table 2). This approach is appealing for the present purposes since it allows higher-order moments to remain fixed. For cases 11–26, a topographic stencil with 64 uniform height, square-based blocks were distributed across the $N_x = N_y = 128$ computational grid (i.e., each block had side length, $L_x/8$; see also Fig. 1b, c). The block heights of groups of blocks were fixed to one of four equivalent values $(h_{o1}, h_{o2}, h_{o3}, h_{o4})$, and these values were systematically varied. These block heights were varied randomly to attain the desired realistic variability of s_k (cases 11–18) and k_u (cases 19–26). For cases 27–46, the cases 1–10 topographic stencil was reused, but the heights of the blocks were varied in pair to manipulate the statistical moments. For example, for cases 39–42, the case 9 topography was used as the base, and then the height of half the blocks was increased while the height of the remaining half was decreased. By introducing this heterogeneity, the skewness was varied systematically. For case 47 to 56, all block heights (within the topographic stencil) were selected with MatLabTM's random number generator (see Fig. 1d).

References

Albertson J, Parlange M (1999) Surface length scales and shear stress: implications for land–atmosphere interaction over complex terrain. Water Resour Res 35:2121–2132

Allen J, Shockling M, Kunkel G, Smits A (2007) Turbulent flow in smooth and rough pipes. Philos Trans R Soc A 365(1852):699–714

Anderson W (2012) An immersed boundary method wall model for high-Reynolds number channel flow over complex topography. Int J Numer Methods Fluids 71:1588–1608

Anderson W (2016) Amplitude modulation of streamwise velocity fluctuations in the roughness sublayer: evidence from large-eddy simulations. J Fluid Mech 789:567–588

Anderson W, Meneveau C (2010) A large-eddy simulation model for boundary-layer flow over surfaces with horizontally resolved but vertically unresolved roughness elements. Boundary-Layer Meteorol 137:397–415

Anderson W, Meneveau C (2011) A dynamic large-eddy simulation model for boundary layer flow over multiscale, fractal-like surfaces. J Fluid Mech 679:288–314

Anderson W, Barros J, Christensen K, Awasthi A (2015a) Numerical and experimental study of mechanisms responsible for turbulent secondary flows in boundary layer flows over spanwise heterogeneous roughness. J Fluid Mech 768:316–347

Anderson W, Li Q, Bou-Zeid E (2015b) Numerical simulation of flow over urban-like topographies and evaluation of turbulence temporal attributes. J Turbul 16(9):809–831

Armenio V, Geurts B, Fröhlich J (2010) Direct and large-eddy simulation VII: Proceedings of the seventh international ERCOFTAC workshop on direct and large-eddy simulation, held at the University of Trieste, 8–10 Sept 2008, vol 13. Springer

Belcher S, Harman I, Finnigan J (2012) The wind in the willows: flows in forest canopies in complex terrain. Annu Rev Fluid Mech 44:479–504

Böhm M, Finnigan JJ, Raupach MR, Hughs D (2013) Turbulence structure within and above a canopy of bluff elements. Boundary-Layer Meteorol 146:393–419

Bou-Zeid E, Meneveau C, Parlange M (2005) A scale-dependent lagrangian dynamic model for large eddy simulation of complex turbulent flows. Phys Fluids 17(2):025,105

Bou-Zeid E, Parlange M, Meneveau C (2007) On the parameterization of surface roughness at regional scales. J Atmos Sci 64:216–227

Castro I (2007) Rough-wall boundary layers: mean flow universality. J Fluid Mech 585:469–485

Chan L, MacDonald M, Chung D, Hutchins N, Ooi A (2015) A systematic investigation of roughness height and wavelength in turbulent pipe flow in the transitionally rough regime. J Fluid Mech 771:743–777

Cheng H, Castro I (2002) Near wall flow over urban-like roughness. Boundary-Layer Meteorol 104:229–259

Cheng H, Hayden P, Robins A, Castro I (2007) Flow over cube arrays of different packing densities. J Wind Eng Ind Aerodyn 95(8):715–740

Cheng WC, Porté-Agel F (2015) Adjustment of turbulent boundary-layer flow to idealized urban surfaces: a large-eddy simulation study. Boundary-Layer Meteorol 155(2):249–270

Chung J, Hagishima A, Ikegaya N, Tanimoto J (2015) Wind-tunnel study of scalar transfer phenomena for surfaces of block arrays and smooth walls with dry patches. Boundary-Layer Meteorol 157(2):219–236

Coceal O, Thomas T, Castro I, Belcher S (2006) Mean flow and turbulence statistics over groups of urban-like cubical obstacles. Boundary-Layer Meteorol 121(3):491–519

Coceal O, Dobre A, Thomas TG, Belcher SE (2007) Structure of turbulent flow over regular arrays of cubical roughness. J Fluid Mech 589:375–409

Counehan J (1971) Wind tunnel determination of the roughness length as a function of the fetch and the roughness density of three-dimensional roughness elements. Atmos Environ 5(8):637–642

De Marchis M, Napoli E (2012) Effects of irregular two-dimensional and three-dimensional surface roughness in turbulent channel flows. Int J Heat Fluid Flow 36:7–17

Fang C, Sill B (1992) Aerodynamic roughness length: correlation with roughness elements. J Wind Eng Ind Aerodyn 41(1):449–460

Flack K, Schultz M (2010) Review of hydraulic roughness scales in the fully rough regime. J Fluids Eng 132(4):041,203

Gardner A (2004) A full-scale investigation of roughness lengths in inhomogeneous terrain and a comparison of wind prediction models for transitional flow regimes. PhD Thesis, Texas Tech University

Garratt JR (1994) The atmospheric boundary layer. Cambridge University Press, Cambridge, 316 pp

Germano M (1992) Turbulence: the filtering approach. J Fluid Mech 238:325–336

Germano M, Piomelli U, Moin P, Cabot W (1991) A dynamic subgrid-scale eddy viscosity model. Phys Fluids A 3:1760–1765

Ghisalberti M (2009) Obstructed shear flows: similarities across systems and scales. J Fluid Mech 641:51

Giometto M, Christen A, Meneveau C, Fang J, Krafczyk M, Parlange M (2016) Spatial characteristics of roughness sublayer mean flow and turbulence over a realistic urban surface. Boundary-Layer Meteorol. doi:10.1007/s10546-016-0157-6

Grimmond C, Oke T (1999) Aerodynamic properties of urban areas derived from analysis of surface form. J Appl Meteorol 38(9):1262–1292

Hagishima A, Tanimoto J, Nagayama K, Meno S (2009) Aerodynamic parameters of regular arrays of rectangular blocks with various geometries. Boundary-Layer Meteorol 132(2):315–337

Hama F (1954) Boundary-layer characteristics for smooth and rough surfaces. Trans Soc Naval Arch Mar Eng 62:333–358

Hansen F (1992) Surface roughness lengths. US Army Research Laboratory, ARL-TR-61

Harmon I, Finnigan JJ (2007) A simple unified theory for flow in the canopy and roughness sublayer. Boundary-Layer Meteorol 123:339–364

Hong J, Katz J, Schultz M (2011) Near-wall turbulence statistics and flow structures over three-dimensional roughness in a turbulent channel flow. J Fluid Mech 667:1–37

Hong J, Katz J, Meneveau C, Schultz M (2012) Coherent structures and associated subgrid-scale energy transfer in a rough-wall channel flow. J Fluid Mech 712:92–128

Ito T, Matsumoto A, Ito T, Motozawa M, Iwamoto K, Kawashima H, Ando H, Senda T, Kawaguchi Y (2011) Experimental investigation on effects of surface roughness geometry affecting to flow resistance. In: ASME-JSME-KSME 2011 joint fluids engineering conference. American Society of Mechanical Engineers, New York, pp 3945–3954

Jackson P (1981) On the displacement height in the logarithmic profile. J Fluid Mech 111:15–25

Jimenez J (2004) Turbulent flow over rough wall. Annu Rev Fluid Mech 36:173

Kanda M (2006) Large-eddy simulations on the effects of surface geometry of building arrays on turbulent organized structures. Boundary-Layer Meteorol 118(1):151–168

Kanda M, Moriizumi T (2009) Momentum and heat transfer over urban-like surfaces. Boundary-Layer Meteorol 131(3):385–401

Kanda M, Moriwaki R, Kasamatsu F (2004) Large-eddy simulation of turbulent organized structures within and above explicitly resolved cube arrays. Boundary-Layer Meteorol 112(2):343–368

Kanda M, Inagaki A, Miyamoto T, Gryschka M, Raasch S (2013) A new aerodynamic parametrization for real urban surfaces. Boundary-Layer Meteorol 148(2):357–377

Kondo H, Inagaki A, Kanda M (2015) A new parametrization of mixing length in an urban canopy derived from a large-eddy simulation database for tokyo. Boundary-Layer Meteorol 156(1):131–144

Krayenhoff E, Santiago JL, Martilli A, Christen A, Oke T (2015) Parametrization of drag and turbulence for urban neighbourhoods with trees. Boundary-Layer Meteorol 156(2):157–189

Kutzbach J (1961) Investigations of the modification of wind profiles by artificially controlled surface roughness. Studies of the three dimensional structure of the planetary boundary layer. Annual Report. Department of Meteorology, University of Wisconsin, Madison, pp 71–113

Lee HM, Wu Y (2015) A Tomo-PIV study of the effects of freestream turbulence on stall delay of the blade of a horizontal-axis wind turbine. Wind Energy 18(7):1185–1205

Leonardi S, Castro I (2010) Channel flow over large cube roughness: a direct numerical simulation study. J Fluid Mech 651:519–539

Leonardi S, Orlandi P, Smalley R, Djenidi L, Antonia R (2003) Direct numerical simulations of turbulent channel flow with transverse square bars on one wall. J Fluid Mech 491:229–238

Lettau H (1969) Note on aerodynamic roughness-parameter estimation on the basis of roughness-element description. J Appl Meteorol 8(5):828–832

Macdonald R, Griffiths R, Hall D (1998) An improved method for the estimation of surface roughness of obstacle arrays. Atmos Environ 32(11):1857–1864

Mara TA, Tarantola S (2012) Variance-based sensitivity indices for models with dependent inputs. Reliab Eng Syst Saf 107:115–121

Mejia-Alvarez R, Christensen K (2010) Low-order representations of irregular surface roughness and their impact on a turbulent boundary layer. Phys Fluids 22:015,106

Meneveau C, Katz J (2000) Scale-invariance and turbulence models for large-eddy simulation. Annu Rev Fluid Mech 32(1):1–32

Millward-Hopkins J, Tomlin A, Ma L, Ingham D, Pourkashanian M (2011) Estimating aerodynamic parameters of urban-like surfaces with heterogeneous building heights. Boundary-Layer Meteorol 141(3):443–465

Millward-Hopkins J, Tomlin A, Ma L, Ingham D, Pourkashanian M (2013) Aerodynamic parameters of a uk city derived from morphological data. Boundary-Layer Meteorol 146(3):447–468

Moody LF (1944) Friction factors for pipe flow. Trans ASME 66(8):671–684

Moser RD, Kim J, Mansour NN (1999) Direct numerical simulation of turbulent channel flow up to Re = 590. Phys Fluids 11(4):943–945

Napoli E, Armenio V, Marchis MD (2008) The effect of the slope of irregularly distributed roughness elements on turbulent wall-bounded flows. J Fluid Mech 613:385–394

Nikuradse J (1950) Laws of flow in rough pipes. National Advisory Committee for Aeronautics, Tech Memo # 1292

Perry A, Schofield W, Joubert P (1969) Rough wall turbulent boundary layers. J Fluid Mech 37:383–413

Placidi M, Ganapathisubramani B (2015) Effects of frontal and plan solidities on aerodynamic parameters and the roughness sublayer in turbulent boundary layers. J Fluid Mech 782:541–566

Pope SB (2000) Turbulent flows. Cambridge University Press, Cambridge, UK, 771 pp

Porté-Agel F, Meneveau C, Parlange M (2000) A scale-dependent dynamic model for large-eddy simulation: application to a neutral atmospheric boundary layer. J Fluid Mech 415:261–284

Ratti C, Sabatino SD, Britter R, Brown M, Caton F, Burian S (2002) Analysis of 3-D urban databases with respect to pollution dispersion for a number of European and American cities. Water Air Soil Pollut Focus 2(5–6):459–469

Ratto M, Tarantola S, Saltelli A (2001) Sensitivity analysis in model calibration: GSA-GLUE approach. Comput Phys Commun 136(3):212–224

Raupach M, Antonia R, Rajagopalan S (1991) Rough-wall turbulent boundary layers. Appl Mech Rev 44:1–25

Raupach M, Finnigan J, Brunet Y (1996) Coherent eddies and turbulence in vegetation canopies: the mixing-layer analogy. Boundary-Layer Meteorol 78:351–382

Rij JV, Belnap B, Ligrani P (2002) Analysis and experiments on three-dimensional, irregular surface roughness. J Fluids Eng 124(3):671–677

Rotach M (1999) On the influence of the urban roughness sublayer on turbulence and dispersion. Atmos Environ 33:4001–4008

Roth M (2000) Review of atmospheric turbulence over cities. Q J R Meteorol Soc 126(564):941–990

Saltelli A (2002) Sensitivity analysis for importance assessment. Risk Anal 22(3):579–590

Saltelli A, Chan K, Scott EM (2000) Sensitivity analysis. Wiley, Oxford, UK, 504 pp

Saltelli A, Annoni P, Azzini I, Campolongo F, Ratto M, Tarantola S (2010) Variance based sensitivity analysis of model output. Design and estimator for the total sensitivity index. Comput Phys Commun 181(2):259–270

Schultz M, Flack K (2009) Turbulent boundary layers on a systematically varied rough wall. Phys Fluids 21(1):015,104

Shockling M, Allen J, Smits A (2006) Roughness effects in turbulent pipe flow. J Fluid Mech 564:267–285

Sigal A, Danberg J (1990) New correlation of roughness density effect on the turbulent boundary layer. AIAA J 28(3):554–556

Su HB, Schmid H, Vogel C, Curtis P (2008) Effects of canopy morphology and thermal stability on mean flow and turbulence statistics observed inside a mixed hardwood forest. Agric For Meteorol 148(6):862–882

Tennekes H, Lumley J (1972) A first course in turbulence. MIT Press, Cambridge, MA, 320 pp

Theurer W (1993) Dispersion of ground-level emissions in complex built-up areas. PhD Thesis, University of Karlsruhe, Germany

Thom A (1971) Momentum absorption by vegetation. Q J R Meteorol Soc 97:414–428

Townsend A (1976) The structure of turbulent shear flow. Cambridge University Press, Cambridge, UK, 429 pp

Wilczek M, Stevens R, Meneveau C (2015) Spatio-temporal spectra in the logarithmic layer of wall turbulence: large-eddy simulations and simple models. J Fluid Mech 769:R1

Wooding R, Bradley E, Marshall J (1973) Drag due to regular arrays of roughness elements of varying geometry. Boundary-Layer Meteorol 5:285–308

Wu Y, Christensen KT (2007) Outer-layer similarity in the presence of a practical rough-wall topology. Phys Fluids 19:085,108

Wu Y, Christensen KT (2010) Spatial structure of a turbulent boundary layer with irregular surface roughness. J Fluid Mech 655:380–418

Wyngaard J (2010) Turbulence in the atmosphere. Cambridge University Press, Cambridge, 393 pp

Xie ZT, Coceal O, Castro I (2008) Large-eddy simulation of flows over random urban-like obstacles. Boundary-Layer Meteorol 129(1):1–23

Yang X (2016) On the mean flow behaviour in the presence of regional-scale surface roughness heterogeneity. Boundary-Layer Meteorol. doi:10.1007/s10546-016-0157-6

Yang XI, Sadique J, Mittal R, Meneveau C (2016) Exponential roughness layer and analytical model for turbulent boundary layer flow over rectangular-prism roughness elements. J Fluid Mech 789:127–165

Yuan J, Piomelli U (2014a) Estimation and prediction of the roughness function on realistic surfaces. J Turbul 15(6):350–365

Yuan J, Piomelli U (2014b) Roughness effects on the reynolds stress budgets in near-wall turbulence. J Fluid Mech 760:R1 (12 pp)

Yuan J, Piomelli U (2015) Numerical simulation of a spatially developing accelerating boundary layer over roughness. J Fluid Mech 780:192–214

Zagarola M, Smits A (1998) Mean-flow scaling of turbulent pipe flow. J Fluid Mech 373:33–79

Zaki SA, Hagishima A, Tanimoto J, Ikegaya N (2011) Aerodynamic parameters of urban building arrays with random geometries. Boundary-Layer Meteorol 138(1):99–120